Environmental Fluid Mechanics (2022) 22:429–446
https://doi.org/10.1007/s10652-021-09813-6

ORIGINAL ARTICLE

Linear stability of sand waves sheared by a turbulent flow

Subhasish Dey[1] · **Rajesh K. Mahato**[1] · **Sk Zeeshan Ali**[2]

Received: 4 June 2021 / Accepted: 31 August 2021 / Published online: 11 September 2021

Abstract
In this paper, the linear stability of sand waves sheared by a turbulent flow is analyzed. The velocity distribution in the streamwise direction is considered to follow the logarithmic law. The modified pressure distribution owing to the streamline curvature induced by the sand waves is employed in the formulation. The pressure distribution is derived using the Boussinesq approximation for the variation of streamline curvature over the flow depth. The flow model is coupled with the sediment transport model to study the stability of sand waves. Both the modes of sediment transport as bedload and suspended load are considered. The linear stability analysis reveals the favorable region for the formation of dunes and antidunes on the plane formed by the Froude number and the dimensionless wavenumber. The region of instability increases with an increase in particle parameter, while it decreases with an increase in relative roughness. The analysis reveals that the sand waves form beyond a limiting Froude number corresponding to the threshold Shields number. The theoretical results compare well with the available experimental data.

Keywords Linear stability · Sand waves · Turbulent flow · Sediment transport

Abbreviations

C	Depth-averaged suspended sediment concentration
C_0	Undisturbed depth-averaged suspended sediment concentration
C_1	Perturbation of depth-averaged suspended sediment concentration
C_r	Reference concentration
$\overline{C}_1, \overline{h}_1, \overline{U}_1, \overline{\eta}_1$	Complex quantities
c	Suspended sediment concentration
D	Mean flow depth
D_*	Particle parameter
d	Median sediment size
d_s	Relative roughness
F	Froude number

✉ Subhasish Dey
sdey@iitkgp.ac.in

[1] Department of Civil Engineering, Indian Institute of Technology Kharagpur, Kharagpur, West Bengal 721302, India

[2] Department of Civil Engineering, Indian Institute of Technology Hyderabad, Sangareddy, Telangana 502284, India

f	Darcy–Weisbach friction factor
f_0	Darcy–Weisbach friction factor corresponding to unperturbed flow
g	Acceleration due to gravity
h	Free surface profile
h_0	Undisturbed free surface profile
h_1	Perturbation of free surface profile
k	Wavenumber
k_s	Roughness height
$\overline{p}$	Time-averaged pressure intensity scaled with mass density of fluid
$\overline{p}_0$	$\overline{p}$ at free surface
q_b	Bedload transport rate
q_s	Suspended load transport rate
R_*	Shear Reynolds number
S_c	Turbulent Schmidt number
s	Relative density
t	Time
U	Depth-averaged velocity
U_0	Undisturbed depth-averaged velocity
U_1	Perturbation of depth-averaged velocity
(u, w)	Instantaneous streamwise and vertical velocity components in (x, z)
$(\overline{u}, \overline{w})$	Time-averaged velocity components in (x, z)
u', w'	Fluctuations of instantaneous velocity components in (x, z)
u_*	Shear velocity
w_s	Terminal fall velocity
(x, z)	Cartesian coordinates
z_0	Zero-velocity level
$\tilde{z}_0$	$z_0/(h-\eta)$
z_r	Reference level
$\tilde{z}_r$	z_r/D
α_1	Exponent
β	Function of $\tilde{z}_0$
δ	Arctan$(\overline{w}/\overline{u})$
$(\varepsilon_x, \varepsilon_z)$	Turbulent diffusivity components in (x, z)
ζ	Rouse number
η	Erodible bed profile
η_0	Undisturbed erodible bed profile
η_1	Perturbation of erodible bed profile
η^*	$\eta + z_0$
Θ	Shields number
Θ_c	Threshold Shields number
κ	von Kármán constant
μ	Friction coefficient
υ	Kinematic viscosity of fluid
Ξ, ξ_1, ξ_2	Functions of $\tilde{z}_0$
ρ_f	Mass density of fluid
ρ_p	Sediment porosity
ρ_s	Mass density of sediment particles
τ_0	Bed shear stress

Ω	Complex quantity
$\mathfrak{R}$	Streamline curvature

1 Introduction

The riverbed sedimentary patterns form as a result of an orderly pattern of scour and deposition triggered by the instability mechanism taking place at the interface of flow and bed. The trough and crest regions of the instigated patterns are subjected to scour and deposition, respectively, and eventually, the patterns reach an equilibrium configuration. The presence of riverbed patterns significantly alters the flow resistance and the nature of sediment transport [1]. Therefore, the origin, development, and dynamics of the riverbed patterns are extensively explored by means of theoretical [2–17], numerical [18–22], and experimental [23–32] researches. Moreover, several comprehensive reviews on the formation of riverbed patterns are reported in the literature [33, 34].

The literature reports that the existing linear stability analyses have employed several flow models, namely potential flow model, shallow water model and rotational flow model [33]. The linear stability analysis seeks the unstable region on the parameter space for the formation of patterns. The theoretical studies on the instability of dunes and antidunes started with the seminal work of Kennedy [2]. He considered a potential flow model for flow over an erodible bed to investigate the instability of the erodible plane bed to dunes and antidunes. The study disclosed the favorable conditions for the formation of dunes and antidunes. Moreover, the analysis revealed the analytical expressions for the wavelength and propagation speed of dunes and antidunes. A look at the sediment continuity equation discloses that a phase lag between the sediment transport (or the bed shear stress) and the bed topography is required to trigger the instability. As the potential flow model does not offer an estimate of the bed shear stress, Kennedy [2] externally provided a phase lag distance to provoke the instability. The potential flow model was further used by Hayashi [4] to explore the instability of sand waves. He presented a model for the sediment transport over a wavy bed and provided an improved explanation of the phase lag between the sediment transport and the bed topography. Moreover, the analysis predicted favorable region for the occurrence of sand waves that nicely agreed with the experimental data.

The rotational and shallow water flow models facilitate the estimation of bed shear stress that causes the instability. Engelund [5] suggested that the flow over a sinusoidal bed can be described by the vorticity transport equation. He performed a linear stability analysis to study the formation of sand waves. The study predicted stability diagrams in Froude number versus dimensionless wavenumber space. The vorticity transport equation was also used by Fredsøe [6] to investigate the stability of flow in a straight alluvial channel. He incorporated the effects of bed inclination on the bedload transport rate. It was discovered that the effects of the bed slope on the bedload transport rate significantly alter the region of instability for the dunes. The observation supports the fact that the bedload is the dominant mode of sediment transport for the formation of dunes, while the suspended sediment transport is required for the formation of antidunes. Richards [7] studied the instability of low Froude number flow over an erodible bed. Unlike the earlier studies, the analysis revealed two distinct modes of instability leading to the formation of ripples and dunes. It was reported that the wavelength of the ripples and dunes scale with the bed roughness and the flow depth, respectively. Colombini [9] suggested that the phase lag between the sediment transport and the bed elevation considerably depends on the level at which the bed

shear stress is to be evaluated. He determined the bed shear stress at the edge of the saltation layer. Such a minor modification was found to remarkably alter the stability diagrams emerging from the linear stability analysis. The analysis of Colombini [9] revealed that the formation of antidunes does not necessarily require the effects of sediment suspension and particle inertia. Further, Colombini and Stocchino [10] performed a weakly nonlinear analysis to predict the finite amplitude of river dunes. Employing the Reynolds averaged Navier–Stokes (RANS) and time-averaged continuity equations, Bose and Dey [11] analyzed the turbulent flow over an undulating sand bed. However, they used the depth-averaged flow model to investigate the instability of sand waves. The analysis disclosed the region of instability in Froude number versus dimensionless wavenumber space. Moreover, Bose and Dey [12] used the same flow model to study the formation of ripples.

With the advent of high-performance computing system, the dynamics of sand waves has been explored by means of the numerical simulations. The study of Tjerry and Fredsøe [35] revealed that the maximum height of dunes coincides with the location of the peak sediment transport. The height and steepness of dunes at equilibrium stage were predicted by the numerical model of Niemann et al. [36]. Khosronejad and Sotiropoulos [21] explored the initiation, growth and evolution of sand waves. They studied the temporal evolutions of the amplitude, wavelength and celerity of sand waves. They also observed that the near-bed sweeps are to initiate the instability of an initially flat sand bed. Liu et al. [22] performed a coupled hydro-morphodynamic simulation to explore the evolution of 3D dunes. They reported that the interaction between the sediment transport and the near-bed flow velocity governs the formation of small sand waves.

The properties of sand waves were also explored through extensive experiments. Simons et al. [25] studied the resistance to flow for different types of bedforms. The laboratory investigations of Kennedy [30] revealed the occurrence of antidunes and their effects on the friction factor and the sediment transport capacity of channels. Guy et al. [31] reported a comprehensive summary of the alluvial bedforms data. In their experiments with different flow conditions, the plane erodible bed eventually changed to ripples, dunes and antidunes. Based on the experimental data of Guy et al. [31], Fredsøe [37] proposed an empirical relation for the ratio of dune amplitude to wavelength. Several empirical relations for the amplitude and wavelength of dunes were also reported in the literature [38–40].

Based on the brief literature survey, it is evident that the mechanism of the formation of sand waves has been explored significantly. However, there remains a scope to study the sensitivity of the stability diagram to the particle parameter and relative roughness. The present work is dedicated to investigate the stability of sand waves, for example, dunes and antidunes. To be specific, dunes are nearly-asymmetrical triangular patterns having a gentle convexly-curved upstream slope and a steep downstream slope equaling the angle of repose of sediment. They appear in the lower flow regime (Froude number < 1), propagating in the downstream direction and remaining out of phase with the free surface profile. On the other hand, antidunes appear with a sinusoidal streamwise profile in the upper flow regime (Froude number > 1), remaining almost in phase with the free surface profile. They can remain stationary or migrate in both the upstream and downstream directions. The geometrical properties of both dunes and antidunes scale with the mean flow depth. The formation of riverbed patterns can be investigated via the dynamic coupling of the flow and the sediment transport.

In the present formulation, an attempt is made, as an advancement of Bose and Dey [11], to obtain a flow model over an undulating sand bed based on the RANS and the time-averaged continuity equations. The streamwise flow velocity is assumed to follow the logarithmic law. The Boussinesq approximation is used to treat the streamline curvature over

the flow depth. The bed shear stress is modelled by considering an improved choice of the friction factor. In addition, combining the formulated flow model with the sediment transport model, a linear stability analysis is performed to study the formation of sand waves. The effects of particle parameter and relative roughness on the stability diagram are explored.

2 Mathematical formulation

2.1 Flow model

Figure 1 depicts a schematic of turbulent shear flow over a mildly undular erodible bed. The bed consists of uniform cohesionless sediment having a median size d. The fluid is considered to be incompressible with a mass density ρ_f and a kinematic viscosity υ. In Fig. 1, a 2D coordinate system (x, z) is considered, where x is the streamwise distance along the mean bed level and z is the vertical distance. The origin of the coordinate system is at the point O. The mean flow depth is denoted by D. The erodible bed and the undular free surface of flow are represented by $\eta(x, t)$ and $h(x, t)$, respectively. Here, t is the time of interest. The streamwise length scale of undulations is considered to be significantly larger than the vertical length scale. The instantaneous velocity components in (x, z) directions at an arbitrary point $A(x, z)$ in the flow domain are denoted by (u, w). Employing the Reynolds decomposition, the instantaneous velocity components (u, w) are expressed as

$$u(x,z,t) = \overline{u}(x,z) + u'(x,z,t), w(x,z,t) = \overline{w}(x,z) + w'(x,z,t) \tag{1}$$

where $\overline{u}$ and $\overline{w}$ are the time-averaged velocity components in (x, z) directions, and u' and w' are the fluctuations of u and w, respectively, with respect to their time-averaged values.

The continuity equation of time-averaged flow is expressed as

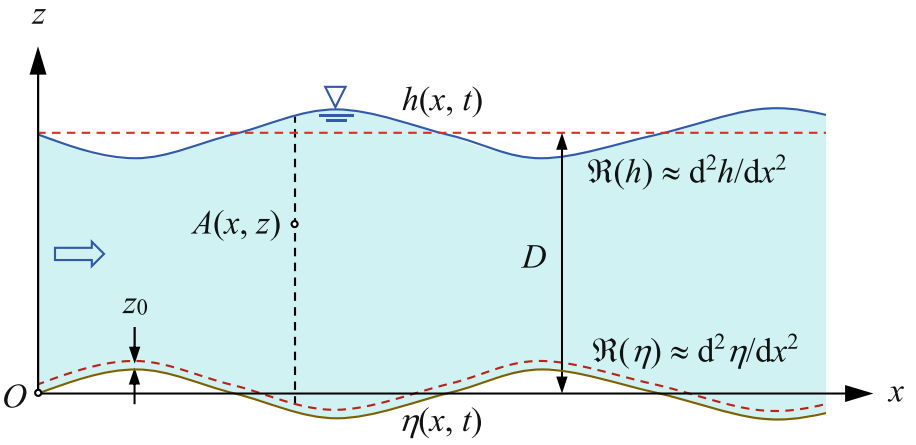

Fig. 1 Schematic of the flow model

$$\frac{\partial \overline{u}}{\partial x} + \frac{\partial \overline{w}}{\partial z} = 0 \tag{2}$$

The RANS equations are expressed as

$$\frac{\partial \overline{u}}{\partial t} + \overline{u}\frac{\partial \overline{u}}{\partial x} + \overline{w}\frac{\partial \overline{u}}{\partial z} = -\frac{\partial \overline{p}}{\partial x} + \upsilon\frac{\partial^2 \overline{u}}{\partial z^2} - \frac{\partial \overline{u'u'}}{\partial x} - \frac{\partial \overline{u'w'}}{\partial z} \tag{3}$$

$$\frac{\partial \overline{w}}{\partial t} + \overline{u}\frac{\partial \overline{w}}{\partial x} + \overline{w}\frac{\partial \overline{w}}{\partial z} = -g - \frac{\partial \overline{p}}{\partial z} + \upsilon\frac{\partial^2 \overline{w}}{\partial x^2} - \frac{\partial \overline{u'w'}}{\partial x} - \frac{\partial \overline{w'w'}}{\partial z} \tag{4}$$

where g is the acceleration due to gravity and $\overline{p}(x, z, t)$ is the time-averaged pressure intensity scaled with the mass density of fluid. To close the physical system, the turbulent stresses are considered to be invariant with the streamwise distance x [11]. This suggests

$$\frac{\partial \overline{u'w'}}{\partial x} \approx 0, \frac{\partial \overline{u'u'}}{\partial x} \approx 0, \frac{\partial \overline{w'w'}}{\partial x} \approx 0 \tag{5}$$

Based on the flow characteristics, the flow field in an open channel can be described by several flow layers. They are the viscous sublayer, buffer layer, turbulent wall-shear layer and turbulent outer layer [41]. In each flow layer, a distinctive law of the streamwise velocity is preserved. However, to get a reasonable analytical solution, a single velocity distribution over the entire flow depth can be adopted. We consider the logarithmic law of velocity distribution over the entire flow depth. The logarithmic law of velocity is expressed as [42]

$$\overline{u} = \frac{u_*}{\kappa}\ln\frac{z-\eta}{z_0} \tag{6}$$

where u_* is the shear velocity, κ is the von Kármán constant (=0.41), and z_0 is the zero-velocity level. Note that in the presence of significant sediment transport, the von Kármán constant slightly deviates from its well-accepted value owing to the reduction of the mixing length of turbulent eddies [43, 44]. This has potential implications on the sediment entrainment [45]. Gaudio et al. [43] and Gaudio and Dey [44] stated that the sediment particles interact with the flow, which drives them, and the bed roughness, which resists them. The particle impact in the near-bed flow zone extracts the momentum from the mean flow, yielding a reduction in the local flow velocity and an increase in the streamwise velocity gradient in the vertical and the Reynolds stresses. The present work considers a constant value of the von Kármán constant in order to simplify this complex interaction. However, in the numerical computations, it was observed that a slight change in the von Kármán constant value has little influence on the results of stability analysis. The z_0 is sensitive to the flow regimes. The flow regimes are classified on the basis of the shear Reynolds number R_* as hydraulically smooth ($R_* \leq 3$), rough ($R_* \geq 70$), and transitional ($3 < R_* < 70$) [41]. The R_* is defined as $R_* = u_* k_s/\upsilon$, where k_s is the roughness height. The k_s can be related to the particle size d as $k_s = \alpha d$, where α is an empirical constant equaling 2.5 [46]. In a hydraulically smooth flow, the zero-velocity level z_0 depends on u_* and υ, while in a hydraulically rough flow, it is solely determined by k_s. In addition, the z_0 in a hydraulically transitional flow can be obtained by the combined effects of smooth and rough flows. However, this study is mainly focused on the rough flow, where $z_0 = k_s/30$. The logarithmic law of velocity distribution in terms of the depth-averaged velocity U is expressed as

$$\overline{u} = \frac{U}{\beta}\ln\frac{z-\eta}{z_0} \text{ with } \beta = -\frac{1}{1-\tilde{z}_0}\ln\tilde{z}_0 - 1 \tag{7}$$

where $\tilde{z}_0 = z_0/(h-\eta)$.

The curvature of the streamlines emerging from the bed undulations induces an acceleration component normal to the flow direction. The amplitude of the undulations is considered to be much smaller than the flow depth. Therefore, the normal acceleration is deemed to be solely convective ($\partial\overline{w}/\partial t \approx 0$) [11, 47, 48]. Using Eq. (2), the normal acceleration can be expressed as

$$\overline{u}\frac{\partial\overline{w}}{\partial x} + \overline{w}\frac{\partial\overline{w}}{\partial z} = \overline{u}^2\frac{\partial}{\partial x}\tan\delta \approx \overline{u}^2\mathfrak{R} \tag{8}$$

where $\tan\delta$ is the slope of the streamline through an arbitrary point $A(x, z)$ in the flow domain and $\mathfrak{R}$ is the curvature of the streamline at $A(x, z)$. The curvatures of the bed and the free surface are approximated as $\mathfrak{R}(\eta) \approx \mathrm{d}^2\eta/\mathrm{d}x^2$ and $\mathfrak{R}(h) \approx \mathrm{d}^2h/\mathrm{d}x^2$. Employing the Boussinesq approximation [49], a linear variation of the streamline curvature between $\mathfrak{R}(\eta)$ and $\mathfrak{R}(h)$ is considered as follows [11, 48]:

$$\mathfrak{R} = \mathfrak{R}(\eta) + [\mathfrak{R}(h) - \mathfrak{R}(\eta)]\frac{z-\eta}{h-\eta} \tag{9}$$

The pressure distribution over the flow depth departs from the hydrostatic law owing to the curvature of the streamlines [11, 12, 41]. Except in the vicinity of the erodible bed, the turbulent stresses always dominate the viscous stresses [11, 48]. Hence, we consider $\upsilon\partial^2\overline{w}/\partial x^2 \ll \partial\tau/\partial x \approx 0$. Using Eq. (8), the integration of the momentum equation (Eq. 4) in the vertical direction yields an expression for the time-averaged pressure distribution as

$$\begin{aligned}\bar{p} = \bar{p}_0 + g(h-z) - \overline{w'w'} + \frac{U^2\mathfrak{R}(\eta)}{\beta}\Bigg[(h-\eta)\left(\ln^2\frac{h-\eta}{z_0} - 2\ln\frac{h-\eta}{z_0} + 2\right)\\ -(z-\eta)\left(\ln^2\frac{z-\eta}{z_0} - 2\ln\frac{z-\eta}{z_0} + 2\right)\Bigg] + \frac{U^2}{\beta(h-\eta)}[\mathfrak{R}(h) - \mathfrak{R}(\eta)]\\ \times\left[\frac{(h-\eta)^2}{2}\left(\ln^2\frac{h-\eta}{z_0} - \ln\frac{h-\eta}{z_0} + \frac{1}{2}\right) - \frac{(z-\eta)^2}{2}\left(\ln^2\frac{z-\eta}{z_0} - \ln\frac{z-\eta}{z_0} + \frac{1}{2}\right)\right]\end{aligned} \tag{10}$$

where $\bar{p}_0$ is the time-averaged pressure intensity at the free surface. In the above, the magnitude of $\overline{w'w'}$ at the free surface is considered to be negligible. Differentiating Eq. (10) with respect to x and integrating over the flow depth produce

$$\int_{\eta^*}^{h}\frac{\partial\bar{p}}{\partial x}dz = g(h-\eta^*)\frac{\partial h}{\partial x} + \frac{1}{\beta}\frac{\partial}{\partial x}\left\{U^2(h-\eta)^2\left[\xi_1\mathfrak{R}(\eta) + \xi_2\mathfrak{R}(h)\right]\right\} \tag{11}$$

where $\eta^* = \eta + z_0$, and ξ_1 and ξ_2 are expressed as

$$\xi_1 = \frac{1-3\tilde{z}_0}{6}\ln^2\tilde{z}_0 + \frac{5-27\tilde{z}_0}{18}\ln\tilde{z}_0 - \frac{7\tilde{z}_0(1-\tilde{z}_0)}{4} + \frac{19(1-\tilde{z}_0^3)}{108} \tag{12}$$

$$\xi_2 = \frac{2-3\tilde{z}_0}{6}\ln^2\tilde{z}_0 + \frac{10-9\tilde{z}_0}{18}\ln\tilde{z}_0 - \frac{\tilde{z}_0}{4} + \frac{19\tilde{z}_0^3}{108} + \frac{2}{27} \tag{13}$$

Using Eq. (11), the momentum equation (Eq. 3) in the streamwise direction is integrated over the flow depth. This yields

$$\frac{\partial U}{\partial t} + \left(\frac{2\Xi}{1-\tilde{z}_0} - 1\right)U\frac{\partial U}{\partial x} + \left(\frac{\Xi}{1-\tilde{z}_0} - 1\right)\frac{U^2}{h-\eta}\cdot\frac{\partial}{\partial x}(h-\eta) + \frac{U^2(h-\eta)}{\beta(1-\tilde{z}_0)}\left[\xi_1\frac{\partial \mathfrak{R}(\eta)}{\partial x} + \xi_2\frac{\partial \mathfrak{R}(h)}{\partial x}\right] + \frac{2U[\xi_1\mathfrak{R}(\eta) + \xi_2\mathfrak{R}(h)]}{\beta(1-\tilde{z}_0)}\cdot\frac{\partial}{\partial x}[U(h-\eta)] + g\frac{\partial h}{\partial x} + \frac{fU^2}{8(1-\tilde{z}_0)(h-\eta)} = 0 \tag{14}$$

where f is the Darcy–Weisbach friction factor and Ξ is expressed as

$$\Xi = \frac{1}{\beta^2}[\ln^2\tilde{z}_0 + 2\ln\tilde{z}_0 + 2(1-\tilde{z}_0)] \tag{15}$$

In the above derivation, the total shear stress vanishes at the free surface, while it equals the bed shear stress on the bed. The bed shear stress τ_0 is expressed in terms of the dynamic pressure as $\tau_0 = f\rho_f U^2/8$. To estimate f, the explicit form of the Colebrook–White equation [50] given by Haaland [51] is used. It is

$$\frac{1}{f^{0.5}} = -0.782\ln\left\{\left[\frac{k_s}{14.8(h-\eta)}\right]^{1.1} + \frac{1.725\upsilon}{U(h-\eta)}\right\} \tag{16}$$

Integrating the continuity equation (Eq. 2) over the flow depth yields

$$\frac{\partial}{\partial t}(h-\eta^*) + \frac{\partial}{\partial x}[U(h-\eta^*)] = 0 \tag{17}$$

In order to study the instability of an erodible bed, the described flow model must be supplemented with the sediment transport model. The sediment transport model is described in the succeeding section.

2.2 Sediment transport model

Depending on the flow conditions, the sediment particles are transported as bedload and suspended load. The particles are transported in rolling and/or sliding modes when the fluid induced bed shear stress just exceeds the threshold bed shear stress [41, 52]. With an increase in bed shear stress, the particles travel along the bed performing brief jumps, called the saltation. The bedload transport is defined as the transport of sediment particles in rolling, sliding, and saltating modes. With a further increase in bed shear stress, the upward diffusion of turbulence brings relatively fine particles into the suspension. In this case, the particles are transported as suspended load. In this study, both the bedload and suspended load sediment transport are taken into account. The advection–diffusion equation of the suspended sediment concentration is expressed as [5, 11]

$$\frac{Dc}{Dt} = w_s\frac{\partial c}{\partial z} + \varepsilon_x\frac{\partial^2 c}{\partial x^2} + \varepsilon_z\frac{\partial^2 c}{\partial z^2} \tag{18}$$

where c is the suspended sediment concentration, w_s is the terminal fall velocity, and ε_x and ε_z are the components of turbulent diffusivity in (x, z) directions, respectively. The w_s is obtained from the empirical formula of Jiménez and Madsen [53] as

$$\frac{w_s}{[(s-1)gd]^{1/2}} = \left(0.954 + \frac{20.48}{D_*^{3/2}}\right)^{-1} \tag{19}$$

where s is the relative density $(=\rho_s/\rho_f)$, ρ_s is the mass density of sediment particles, and D_* is the particle parameter $\{=d[(s-1)g/\upsilon^2]^{1/3}\}$. The ε_x and ε_y are obtained as follows [54, 55]:

$$\varepsilon_x = 7.25u_*D\left(\frac{U}{u_*}\right)^{1/4}, \ \varepsilon_y = \frac{u_*D}{15} \tag{20}$$

The integration of the advection–diffusion equation over the flow depth gives

$$\frac{\partial}{\partial t}[(h-\eta^*)C] + \frac{\partial}{\partial x}[(h-\eta^*)UC] = \varepsilon_x\frac{\partial^2}{\partial x^2}[(h-\eta^*)C] \tag{21}$$

where C is the depth-averaged suspended sediment concentration. The total load is the sum of the bedload and the suspended load. The dynamics of the bed evolution can be obtained from the Exner's equation. It is

$$\frac{\partial}{\partial t}[(h-\eta^*)C] + (1-\rho_p)\frac{\partial \eta}{\partial t} + \frac{\partial q_b}{\partial x} + \frac{\partial q_s}{\partial x} = 0 \tag{22}$$

where ρ_p is the sediment porosity, q_b is the bedload transport rate, and q_s is the suspended load transport rate.

The bedload transport rate is obtained from the empirical formula of Meyer-Peter and Müller [56] as

$$\frac{q_b}{[(s-1)gd^3]^{1/2}} = 8\left(\Theta - \Theta_c - \mu\frac{\partial \eta}{\partial x}\right)^{3/2} \tag{23}$$

where Θ is the Shields number representing the dimensionless bed shear stress $\{=u_*^2/[(s-1)gd]\}$, μ is the friction coefficient (≈ 0.1), and Θ_c is the threshold Shields number. The estimation of Θ_c from a micro-mechanical analysis at the bed particle level is rather complex [57, 58]. However, to simplify the analysis, Θ_c is expressed as a function of particle parameter using the empirical formulas [59, 60]. In this study, the Θ_c is obtained as follows [59]:

$$\Theta_c = KD_*^{\alpha_1} \tag{24}$$

where the coefficient K and the exponent α_1 are given in Wu and Wang [59].

It is worth mentioning that the sediment suspension occurs when the Shields number exceeds its threshold of sediment suspension. The suspended load transport rate can be obtained from the integration of the product of sediment concentration and streamwise flow velocity over the suspension layer. Using Eq. (21), Eq. (22) can be expressed as

$$(1-\rho_p)\frac{\partial \eta}{\partial t}+\varepsilon_x\frac{\partial^2}{\partial x^2}[(h-\eta^*)C]+12[(s-1)gd^3]^{1/2}\left(\frac{fU^2}{8(s-1)gd}-\Theta_c-\mu\frac{\partial h}{\partial x}\right)^{1/2}$$
$$\times\left[\frac{2f}{8(s-1)gd}U\frac{\partial U}{\partial x}+\frac{U^2}{8(s-1)gd}\frac{\partial f}{\partial x}-\mu\frac{\partial^2 h}{\partial x^2}\right]=0 \tag{25}$$

Equations (14), (17), (21), and (25) govern the entire dynamics of the physical system.

It is important to mention that the present formulation is supplemented by various empirical formulas. However, it was found that the model results remain almost insensitive to various choices of empirical relations.

3 Linear stability analysis

To perform the stability analysis, the key variables are expanded as

$$(\eta,h,U,C)=(\eta_0,h_0,U_0,C_0)+(\eta_1,h_1,U_1,C_1) \tag{26}$$

where subscripts '0' and '1' represent the undisturbed and perturbed states of a variable, respectively. The depth-averaged suspended sediment concentration C_0 is expressed as

$$C_0=C_r\frac{1-\exp[-6.15\zeta(1-\tilde{z}_r)]}{6.15\zeta(1-\tilde{z}_r)} \tag{27}$$

where C_r is the reference concentration, $\tilde{z}_r=z_r/D$, z_r is the reference level, ζ is the Rouse number ($=S_c w_s/\kappa u_*$), and S_c is the turbulent Schmidt number (≈ 1). The above equation is obtained from the depth-averaging of the distribution of suspended sediment concentration given by Lane and Kalinske [55]. The C_r and z_r are obtained from the empirical formulas of van Rijn [61] as

$$C_r=0.015\frac{d}{z_r}\left(\frac{\Theta}{\Theta_c}-1\right)^{3/2}D_*^{-0.3} \tag{28}$$

$$z_r(k_s<0.01D)=0.01D, z_r(k_s\geq 0.01D)=k_s \tag{29}$$

For dunes and antidunes, the perturbations must be of the following form [11]:

$$(\eta_1,h_1,U_1,C_1)=(\bar{\eta}_1,\bar{h}_1,\bar{U}_1,\bar{C}_1)\exp(-\Omega t)\exp(ikx) \tag{30}$$

where i is the imaginary unit [$=(-1)^{1/2}$], k is the wavenumber and Ω is a complex quantity whose real and imaginary parts represent the growth rate and the frequency of perturbations, respectively. Using Eqs. (26) and (30), Eqs. (14), (17), (21), and (25) produce a set of linear algebraic equations as follows:

$$\left[\frac{ikU_0^2}{D}\left(\frac{\Xi}{1-\tilde{z}_0}-1\right)-\frac{ik^3\xi_2 DU_0^2}{\beta(1-\tilde{z}_0)}-\frac{f_0U_0^2}{8(1-\tilde{z}_0)D^2}+ikg\right]\overline{h}_1+\left[\frac{f_0U_0^2}{8(1-\tilde{z}_0)D^2}\right.$$
$$\left.-\frac{ik^3\xi_1 DU_0^2}{\beta(1-\tilde{z}_0)}-\frac{ikU_0^2}{D}\left(\frac{\Xi}{1-\tilde{z}_0}-1\right)\right]\overline{\eta}_1+\left[-\Omega+ikU_0\left(\frac{2\Xi}{1-\tilde{z}_0}-1\right)+\frac{2f_0U_0}{8(1-\tilde{z}_0)D}\right]\overline{U}_1=0 \tag{31}$$

$$(-\Omega+ikU_0)\bar{h}_1-(-\Omega+ikU_0)\bar{\eta}_1+ikD\bar{U}_1=0 \tag{32}$$

$$\begin{aligned}&\left(-\frac{\Omega C_0}{D}+\frac{ikC_0U_0}{D}+\frac{k^2\varepsilon_x C_0}{D}\right)\bar{h}_1\\&+\left(\frac{\Omega C_0}{D}-\frac{ikC_0U_0}{D}-\frac{k^2\varepsilon_x C_0}{D}\right)\bar{\eta}_1\\&+ikC_0\bar{U}_1+(-\Omega+ikU_0+k^2\varepsilon_x)\bar{C}_1=0\end{aligned} \tag{33}$$

$$\left[\frac{ik\mathfrak{F}_1\mathfrak{F}_2\mathfrak{F}_4U_0^2}{8(s-1)gd}-k^2\varepsilon_x C_0\right]\overline{h}_1+\left[k^2\varepsilon_x C_0+\mu k^2-(1-\rho_p)\Omega-\frac{ik\mathfrak{F}_1\mathfrak{F}_2\mathfrak{F}_4U_0^2}{8(s-1)gd}\right]\overline{\eta}_1$$
$$+\left[\frac{2ik\mathfrak{F}_4f_0U_0+ik\mathfrak{F}_1\mathfrak{F}_3\mathfrak{F}_4U_0^2}{8(s-1)gd}\right]\overline{U}_1-k^2\varepsilon_x D\overline{C}_1=0 \tag{34}$$

where f_0 is the Darcy–Weisbach friction factor corresponding to the unperturbed flow and the coefficients $\mathfrak{F}_1$, $\mathfrak{F}_2$, $\mathfrak{F}_3$ and $\mathfrak{F}_4$ are as follows:

$$\begin{aligned}\mathfrak{F}_1&=-1.564\left[\left(\frac{k_s}{14.8D}\right)^{1.1}+\frac{1.725\upsilon}{U_0D}\right]^{-1}\left\{0.782\ln\left[\left(\frac{k_s}{14.8D}\right)^{1.1}+\frac{1.725\upsilon}{U_0D}\right]\right\}^{-3},\\\mathfrak{F}_2&=-\frac{1.1}{D}\left(\frac{k_s}{14.8D}\right)^{1.1}-\frac{1.725\upsilon}{U_0D^2},\\\mathfrak{F}_3&=-\frac{1.725\upsilon}{DU_0^2},\\\mathfrak{F}_4&=12[(s-1)gd^3]^{1/2}\left[\frac{f_0U_0^2}{8(s-1)gd}-\Theta_c\right]^{1/2}\end{aligned} \tag{35}$$

Equations (31)–(34) can be expressed as

$$a_{m1}\overline{h}_1+a_{m2}\overline{\eta}_1+a_{m3}\overline{U}_1+a_{m4}\overline{C}_1=0 \tag{36}$$

where $m=1$ to 4. The algebraic system of equations produces the following dispersion relation:

$$\begin{aligned}&a_{11}a_{22}(a_{33}a_{44}-a_{34}a_{43})-a_{11}a_{23}(a_{32}a_{44}-a_{34}a_{42})-a_{12}a_{21}(a_{33}a_{44}-a_{34}a_{43})\\&+a_{12}a_{23}(a_{31}a_{44}-a_{34}a_{41})+a_{13}a_{21}(a_{32}a_{44}-a_{34}a_{42})-a_{13}a_{22}(a_{31}a_{44}-a_{34}a_{41})=0\end{aligned} \tag{37}$$

Equation (37) is a quartic equation in Ω, which can be solved numerically. The solution yields four values of Ω. The perturbations grow or decay with time if Re(Ω) is negative or positive, respectively.

4 Results and discussion

To compute the model results, the data $\rho_f = 1000$ kg m^{-3}, $\rho_s = 2650$ kg m^{-3}, $\rho_p = 0.4$, $\upsilon = 10^{-6}$ m^2 s^{-1}, and $g = 9.81$ m s^{-2} are considered. The stability diagram can be shown on Froude number [$F = U/(gD)^{1/2}$] versus dimensionless wavenumber (kD) plane. A typical stability diagram delimits the stable and unstable regions.

For a rough flow, the stability diagram involves two key parameters: the particle parameter D_* and the relative roughness d_s ($=d/D$). The former reflects the role of the sediment size, while the latter signifies the effects of frictional resistance. Figure 2 depicts the stability curves for a given relative roughness d_s ($=d/D$) and different particle parameters D_*. An increase in particle parameter represents an increase in sediment size. The limiting broken line in Fig. 2, representing $F \approx 0.22$, corresponds to the threshold Shields number, which is the Shields number required for the initiation of sediment particle motion. Hence, below this line, the formation of dunes and antidunes is not possible within the grey region. For a given D_*, above the broken line, the interior and exterior portions of the curves denote the unstable and stable regions, respectively. It is worth mentioning that for an arbitrary point (kD, F) lying within the unstable region, at least one root of the dispersion relation (Eq. 37) possesses negative real part. On the other hand, all the roots within the stable region are characterized by the positive real part. The roots do not exist below the broken line with the grey region. It is evident that, for a given d_s and D_*, the unstable region is confined to a left bound curve, a right bound curve, and the limiting broken line (Fig. 2). As the D_* increases, the right bound curve shifts toward the longer wavenumbers, enlarging the region of instability. This may be due to the destabilizing effects associated with the coarse

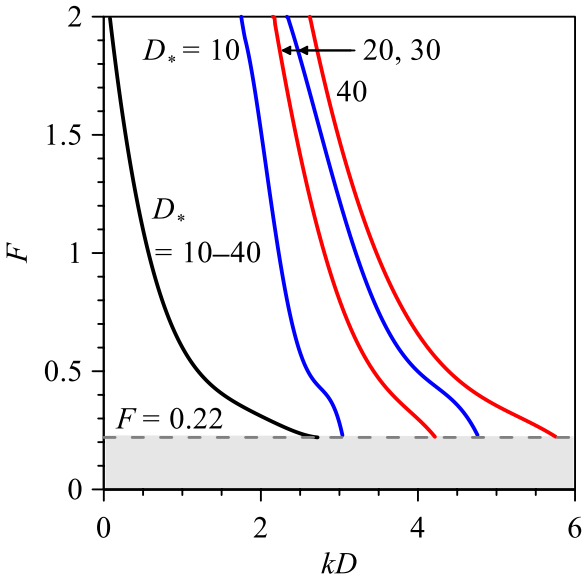

Fig. 2 Stability diagrams for relative roughness $d_s = 0.002$ and different values of particle parameter $D_* = 10$, 20, 30, and 40. For a given D_*, the interior and exterior portions of the curves (above the broken line) denote the unstable and stable regions, respectively. The broken line represents the threshold of the formation of sand waves

sediment size. On the other hand, the left bound curve appears to be a single curve, as the left bound curves for different D_* collapse on a single line. This suggests that for a given Froude number and relative roughness, the limit of the formation of dunes and antidunes in the long-wavelength range is insensitive to the sediment size. However, the limit of the formation of dunes and antidunes in the short-wavelength range varies with the sediment size. Moreover, it appears that the shifting of the right bound curve for a given D_* is more prominent in a subcritical flow than that in a supercritical flow.

The stability curves for a given particle parameter D_* and different relative roughness values d_s are furnished in Fig. 3. An increase in relative roughness for a given sediment size characterizes a decrease in flow depth. For a given d_s, above the broken lines (red and blue), the inner and outer spaces separated by the curves denote the unstable and stable regions, respectively. In Fig. 3, the broken lines represent the limiting Froude numbers for a given D_* and d_s, respectively. It is apparent that the limiting Froude number increases with an increase in d_s, as the friction factor changes. Furthermore, as the d_s increases, the right bound curve moves toward the smaller wavenumbers and reduces the region of instability. It is also evident that the position of left bound curve remains invariant with d_s. This suggests that for a given Froude number and sediment size, the limit of the formation of dunes and antidunes in the long-wavelength range is insensitive to the relative roughness. However, the limit of the formation of dunes and antidunes in the short-wavelength range varies with the relative roughness. Similar to Fig. 2, the shifting of the right bound curve for a given d_s appears to be more prominent in a subcritical flow than that in a supercritical flow.

Figure 4 offers a comparison of the theoretical result obtained from the present formulation with the experimental data of various researchers. The experiments were carried out over broad ranges of d_s (0.0003 to 0.025) and D_* (2 to 36). However, the present study predicts the region of instability for a specific choice of d_s and D_*. Hence, based on the range of the available experimental data, we consider the average values of d_s and D_* as $d_s = 0.003$ and $D_* = 15$, respectively. This choice makes possible to capture most of the

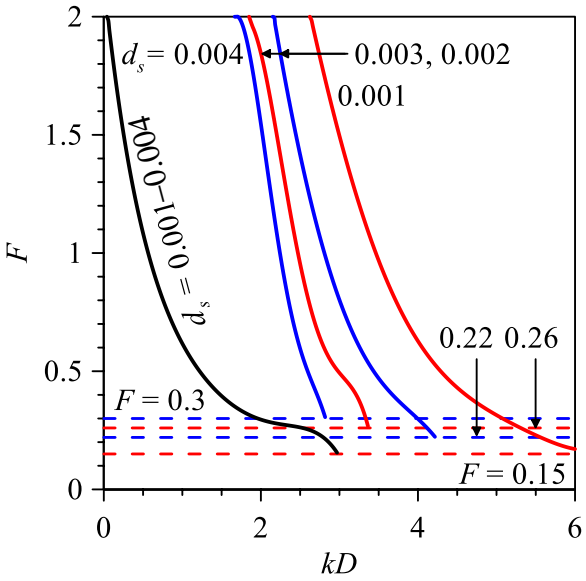

Fig. 3 Stability diagrams for particle parameter $D_* = 20$ and different values of relative roughness $d_s = 0.001$, 0.002, 0.003, and 0.004. For a given D_*, the interior and exterior portions of the curves (above the broken lines) denote unstable and stable regions, respectively. The broken line, for a given Froude number, represents the threshold of the formation of sand waves

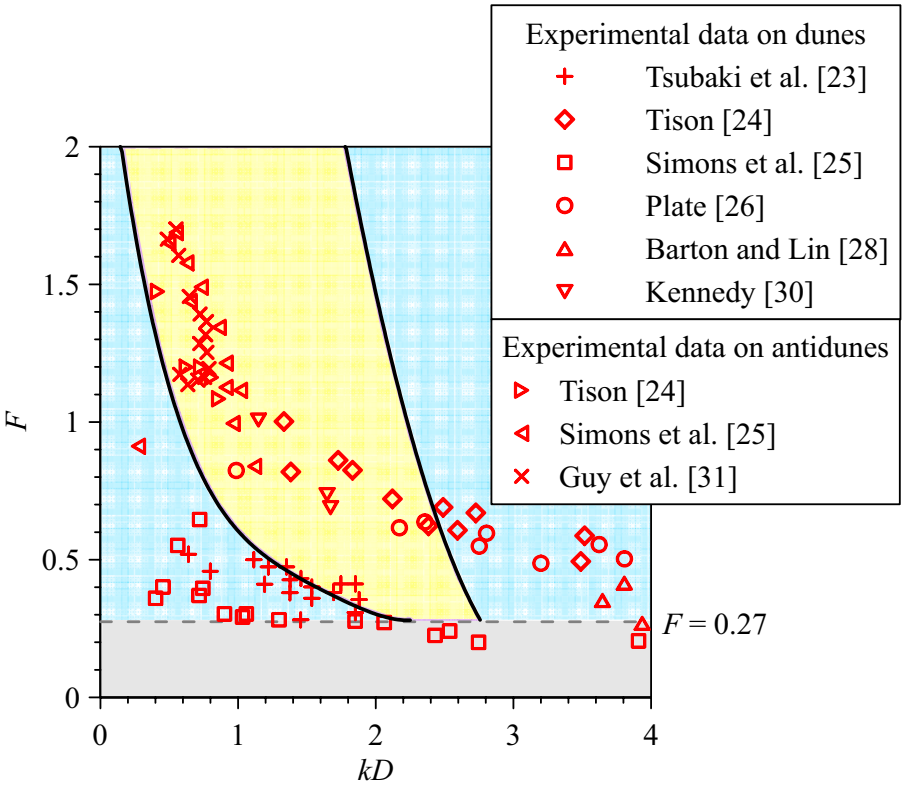

Fig. 4 Comparison of the stability diagram obtained from the present formulation with the available experimental data. The relative roughness d_s and particle parameter D_* are taken as 0.003 and 15, respectively. The unstable region obtained from the present formulation is enclosed by the black lines and the broken line, given by $F = 0.27$

experimental data. It is obvious that most of the experimental data belong to the region above the limiting broken line ($F = 0.27$), being in conformity with the present formulation. Most of the experimental data for smaller Froude numbers ($F < 1$) correspond to dunes, while those for larger Froude numbers ($F > 1$) relate to antidunes. Most of the experimental data fall within the unstable region (marked in yellow). However, some data of dunes lie outside the unstable region. This may be attributed to the fact that the unstable region in Fig. 4 is obtained by considering a specific choice of parameters ($d_s = 0.003$ and $D_* = 15$). Another reason for the data scattering could be that the experimental observations were taken when the sand waves became fully-developed. The development of sand waves leads to a considerable increase in the flow resistance, while in the present analysis, the flow resistance is obtained for an initial plane bed.

Figure 5 furnishes a comparison of the stability diagram obtained from the present formulation with those reported by Kennedy [2], Hayashi [4], and Bose and Dey [11]. Akin to Fig. 4, $d_s = 0.003$ and $D_* = 15$ are considered for the theoretical analysis. In Fig. 5, the $F_a(kD)$ and $F_m(kD)$ curves represent the largest and smallest Froude numbers required for the development of dunes and antidunes, respectively, and the maximum Froude number for the formation of long-crested patterns [2]. According to Hayashi [4], the conditions for

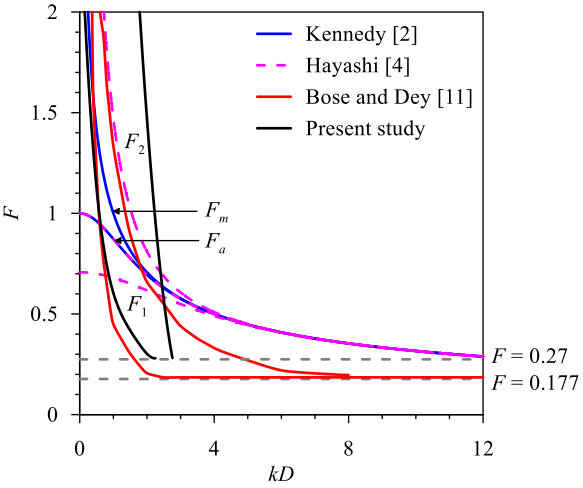

Fig. 5 Comparison of the present formulation with the existing analytical models of Kennedy [2], Hayashi [4], and Bose and Dey [11]. The region enclosed by the solid black lines (above $F=0.27$) denotes the unstable region obtained from the present formulation. The interior of the solid red lines (above $F=0.177$) represents the unstable region predicted by Bose and Dey [11]. Kennedy's [2] predictions: $F=F_a$ denote the largest (or smallest) Froude number for the formation of dunes (or antidunes) and $F=F_m$ is the largest Froude number for the formation of long-crested patterns. Hayashi's [4] predictions: dunes (or antidunes) form for $F<F_1$ (or $F_a<F<F_2$) and plane bed occurs for $F_1<F<F_a$ and $F_2<F$

the occurrence of dunes and antidunes are $F<F_1$ and $F_a<F<F_2$, respectively, and those of plane bed are $F_1<F<F_a$ and $F_2<F$ (see Fig. 5). The region bounded by the red lines and the broken line, representing $F=0.177$, characterizes the unstable region obtained by Bose and Dey [11]. The unstable region obtained from the present formulation is enclosed by the black lines and the broken line, representing $F=0.27$. The broken line represents the limiting curve below which the formation of sand waves is inhibited. In this study, the limiting line for the occurrence of sand waves shifts toward larger flow Froude number owing to the precise estimation of the threshold Shields number [11].

It is apparent from Fig. 5 that the unstable region predicted by the present formulation agrees well with those obtained by earlier theoretical studies. It is worth mentioning that the studies of Kennedy [2] and Hayashi [4] reported the conditions for the occurrence of sand waves. However, they paid little attention to the sensitivity of the lower limit of the formation of sand waves. Bose and Dey [11] reported the lower limit of the formation of sand waves below which the formation of sand waves is inhibited. This study gives a better estimation of the lower limit for the formation of sand waves owing to the precise estimation of the threshold Shields parameter, as adopted in the mathematical analysis.

5 Conclusions

Based on the RANS and the time-averaged continuity equations, a linear stability analysis of sand waves sheared by a turbulent flow is carried out. The streamwise flow velocity is considered to follow the logarithmic law. The developed flow model is coupled with the sediment transport model by means of the Exner equation and the advection–diffusion

equation of sediment suspension. The formation of sand waves is possible above a limiting Froude number corresponding to the threshold Shields number. The region of instability enlarges as the particle parameter increases. This is because of the rightward shifting of the right bound curve to destabilize longer wavenumbers. The unstable region shrinks as the relative roughness increases owing to the leftward switching of right bound curve that stabilizes the smaller wavenumbers. On the contrary, the left bound curve remains independent of the relative roughness. The theoretical curves compare well with the experimental data.

In essence, this study offers an understanding of the instability of sand waves sheared by a turbulent flow, elucidating the role of particle size and relative roughness. However, the study is grounded on the depth-averaged flow model. To gain more insights into the instability mechanism, a rotational flow model can be developed as a future scope of research.

Acknowledgements The first author acknowledges the J C Bose Fellowship Award [Funded by DST, Science and Engineering Research Board (SERB), Grant No. JCB/2018/000004] in pursuing this work.

References

1. Venditti JG, Church M, Bennett SJ (2006) On interfacial instability as a cause of transverse subcritical bed forms. Water Resour Res 42(7):W07423
2. Kennedy JF (1963) The mechanics of dunes and antidunes in erodible-bed channels. J Fluid Mech 16(4):521–544
3. Reynolds AJ (1965) Waves on the erodible bed of an open channel. J Fluid Mech 22(1):113–133
4. Hayashi T (1970) Formation of dunes and antidunes in open channels. J Hydraul Div 96(2):357–366
5. Engelund F (1970) Instability of erodible beds. J Fluid Mech 42(2):225–244
6. Fredsøe J (1974) On the development of dunes in erodible channels. J Fluid Mech 64(1):1–16
7. Richards KJ (1980) The formation of ripples and dunes on an erodible bed. J Fluid Mech 99(3):597–618
8. Colombini M, Seminara G, Tubino M (1987) Finite-amplitude alternate bars. J Fluid Mech 181(August):213–232
9. Colombini M (2004) Revisiting the linear theory of sand dune formation. J Fluid Mech 502(March):1–16
10. Colombini M, Stocchino A (2008) Finite-amplitude river dunes. J Fluid Mech 611(September):283–306
11. Bose SK, Dey S (2009) Reynolds averaged theory of turbulent shear flows over undulating beds and formation of sand waves. Phys Rev E 80(3):036304
12. Bose SK, Dey S (2012) Instability theory of sand ripples formed by turbulent shear flows. J Hydraul Eng 138(8):752–756
13. Colombini M, Stocchino A (2011) Ripple and dune formation in rivers. J Fluid Mech 673(April):121–131
14. Colombini M, Stocchino A (2012) Three-dimensional river bed forms. J Fluid Mech 695(March):63–80
15. Ali SZ, Dey S (2021) Interfacial instability of sand patterns induced by turbulent shear flow. Int J Sed Res 36(4):449–456
16. Ali SZ, Dey S (2021) Instability of large-scale riverbed patterns. Phys Fluids 33(1):015109
17. Mahato RK, Ali SZ, Dey S (2021) Hydrodynamic instability of free river bars. Phys Fluids 33(4):045105
18. Defina A (2003) Numerical experiments on bar growth. Water Resour Res 39(4):1092
19. Chou Y-J, Fringer OB (2010) A model for the simulation of coupled flow-bed form evolution in turbulent flows. J Geophys Res Oceans 115(C10):C10041
20. Siviglia A, Stecca G, Vanzo D, Zolezzi G, Toro EF, Tubino M (2013) Numerical modelling of two-dimensional morphodynamics with applications to river bars and bifurcations. Adv Water Resour 52(February):243–260

21. Khosronejad A, Sotiropoulos F (2014) Numerical simulation of sand waves in a turbulent open channel flow. J Fluid Mech 753(August):150–216
22. Liu Y, Fang H, Huang L, He G (2019) Numerical simulation of the production of three-dimensional sediment dunes. Phys Fluids 31(9):096603
23. Tsubaki T, Kawasumi T, Yasutomi T (1953) On the influence of sand ripples upon the sediment transport in open channels. Rep Res Inst Appl Mech Kyushu Univ 2:241–256
24. Tison LH (1949) Origine des ondes de sable et des bancs de sable sous l'action des courants. Trans Int Ass for Hyd Structures Research, Third Meeting, Grenoble, France
25. Simons DB, Richardson EV, Albertson ML (1961) Flume studies using medium sand (0.45 mm). Geological Survey Water-Supply Paper No 1498-A, US GPO, Washington, DC
26. Plate EJOF (1957) Laboratory studies on the beginning of sediment ripple formation in an alluvial channel. Masters Thesis, Colorado State University
27. Brooks NH (1954) Laboratory studies of the mechanics of streams flowing over a movable bed of fine sand. Doctoral Thesis, California Institute of Technology
28. Barton JR, Lin PN (1955) A study of sediment transport in alluvial channels. Rep No 55JRB2, Colorado A and M College, Ft. Collins, Colorado
29. Laursen EM (1958) The total sediment load of streams. J Hydraul Div 84(1):1–36
30. Kennedy JF (1961) Stationary waves and antidunes in alluvial channels. Rep No KH-R-2, W M Keck Laboratory of Hydraulics and Water Resources, California Institute of Technology
31. Guy HP, Simons DB, Richardson EV (1966) Summary of alluvial channel data from flume experiments 1956–61. Geol Survey Prof Paper 462-I: 1–96
32. Redolfi M, Welber M, Carlin M, Tubino M, Bertoldi W (2020) Morphometric properties of alternate bars and water discharge: a laboratory investigation. Earth Surf Dyn 8(3):789–808
33. Dey S, Ali SZ (2020) Fluvial instabilities. Phys Fluids 32(6):061301
34. Seminara G (2010) Fluvial sedimentary patterns. Annu Rev Fluid Mech 42:43–66
35. Tjerry S, Fredsøe J (2005) Calculation of dune morphology. J Geophys Res 110(F4):F04013
36. Niemann SL, Fredsøe J, Jacobsen NG (2011) Sand dunes in steady flow at low Froude numbers: dune height evolution and flow resistance. J Hydraul Eng 137(1):5–14
37. Fredsøe J (1975) The friction factor and height-length relations in flow over a dune-covered bed. Progress Report Number 37, Institute of Hydrodynamic and Hydraulic Engineering (ISVA), Technical University of Denmark, Kongens Lyngby
38. van Rijn LC (1984) Sediment transport, part III: bed forms and alluvial roughness. J Hydraul Eng 110(12):1733–1754
39. Yalin MS (1977) Mechanics of sediment transport. Pergamon, Oxford
40. Julien PY, Klaassen GJ (1995) Sand-dune geometry of large rivers during floods. J Hydraul Eng 121(9):657–663
41. Dey S (2014) Fluvial hydrodynamics: Hydrodynamic and sediment transport phenomena. Springer-Verlag, Berlin, Germany
42. Schlichting H, Gersten K (2000) Boundary layer theory. Springer, Berlin
43. Gaudio R, Miglio A, Dey S (2010) Non-universality of von Kármán's κ in fluvial streams. J Hydraul Res 48(5):658–663
44. Gaudio R, Dey S (2013) Evidence of non-universality of von Kármán's κ. In: Rowinski P (ed) Experimental and Computational Solutions of Hydraulic Problems. Springer, Berlin, pp 71–83
45. Dey S, Ali SZ (2019) Bed sediment entrainment by streamflow: state of the science. Sedimentology 66(5):1449–1485
46. Engelund F, Hansen E (1967) A monograph on sediment transport in alluvial streams. Danish Technical Press, Copenhagen
47. Bose SK, Dey S (2007) Curvilinear flow profiles based on Reynolds averaging. J Hydraul Eng 133(9):1074–1079
48. Ali SZ, Dey S (2016) Theory of turbulent flow over a wavy boundary. J Hydraul Eng 142(6):04016006
49. Jaeger C (1957) Engineering fluid mechanics. Saint Martin's Press, New York
50. Colebrook CF, White CM (1937) Experiments with fluid friction in roughened pipes. Proc R Soc A 161(August):367–381
51. Haaland SE (1983) Simple and explicit formulas for the friction factor in turbulent flow. J Fluids Eng 105(5):89–90
52. van Rijn LC (1984) Sediment transport, part I: bed load transport. J Hydraul Eng 110(10):1431–1456
53. Jiménez JA, Madsen OS (2003) A simple formula to estimate settling velocity of natural sediments. J Waterw Port Coastal Ocean Eng 129(2):70–78

54. Thackston EL, Krenkel PA (1967) Longitudinal mixing in natural streams. J Sanit Eng Div 93(5):67–90
55. Lane EW, Kalinske AA (1941) Engineering calculations of suspended sediment. Trans Am Geophys Union 20(3):603–607
56. Meyer-Peter E, Müller R (1948) Formulas for bed-load transport. Proc Second Meet Int Assoc Hydraulic Res Stockholm Sweden 3:39–64
57. Ali SZ, Dey S (2016) Hydrodynamics of sediment threshold. Phys Fluids 28(7):075103
58. Dey S, Ali SZ (2018) Advances in modeling of bed particle entrainment sheared by turbulent flow. Phys Fluids 30(6):061301
59. Wu W, Wang SSY (1999) Movable bed roughness in alluvial rivers. J Hydraul Eng 125(12):1309–1312
60. Cao Z, Pender G, Meng J (2006) Explicit formulation of the Shields diagram for incipient motion of sediment. J Hydraul Eng 132(10):1097–1099
61. van Rijn LC (1984) Sediment transport, part II: suspended load transport. J Hydraul Eng 110(11):1613–1641